IOP Publishing Nano Express 6 (2025) 015001 https://doi.org/10.1088/2632-959X/ad9f86

NANO EXPRESS

PAPER

Microstructural, morphological, and optical properties of Fe_2O_3 nanoparticles obtained from Fe-MIM MOF

Olalekan C Olatunde[1,*], **Murendeni P Ravele**[1], **Tunde L Yusuf**[2] and **Damian C Onwudiwe**[1]

[1] Department of Chemistry, School of Physical and Chemical Sciences, Faculty of Natural and Agricultural Sciences, North-West University, Mafikeng Campus, Private Bag X2046, Mmabatho 2735, South Africa

[2] Department of Chemistry, Faculty of Natural and Agricultural Sciences, University of Pretoria, Private Bag X20, Hatfield 0028, Pretoria, South Africa

[*] Author to whom any correspondence should be addressed.

E-mail: 32587139@mynwu.ac.za

Keywords: X-ray diffraction, Williamson-Hall analysis, Scherrer plot, Size Strain plot, Halder-Wagner, UV-vis spectroscopy

OPEN ACCESS

RECEIVED
25 September 2024

REVISED
4 December 2024

ACCEPTED FOR PUBLICATION
16 December 2024

PUBLISHED
7 January 2025

Abstract

This study explores the microstructural, morphological, and optical properties of Fe_2O_3 nanoparticles synthesized from the pyrolysis of ZIF-8 like Fe-2-methyl imidazole (MIM) metal–organic frameworks (MOFs). Using X-ray diffraction (XRD) profile analysis methods, including the modified Scherrer, Williamson–Hall (W-H), size strain plot, and Halder-Wagner methods, the impact of annealing temperature on the microstructural parameters and crystal defects of the obtained Fe_2O_3 nanoparticles was investigated. The nanoparticles exhibited high crystallinity and a rhombohedral α-Fe_2O_3 phase. Morphological analysis through transmission electron microscopy (TEM) revealed distinct structural features, while UV–vis spectroscopy was employed to examine their optical properties. The results indicated that higher annealing temperatures enhance crystallinity, reduce defect density, and improve atomic mobility. This comprehensive analysis provides valuable insights into the synthesis-structure–property relationships of Fe_2O_3 nanoparticles, highlighting their potential applications in applications such as gas sensing and photocatalysis.

1. Introduction

Hematite (α-Fe_2O_3) is a widely studied iron oxide phase that has attracted significant research interest because of its interesting physical and environmental properties, such as non-toxicity, biocompatibility, and remarkable stability under ambient conditions [1, 2]. The compound crystallizes in the rhombohedral crystal system, and space group, R-3c. It is a n-type semiconductor, with a band gap energy of ~2.2 eV. This characteristic allows hematite to be utilized in fields such as photocatalysis [3, 4], lithium-ion batteries [5], gas sensors [6], solar cells [7], pigments [8], and rechargeable Fe/air batteries [9, 10].

Several techniques have been developed to produce α-Fe_2O_3 nanoparticles, such as sol–gel [11–13], thermal decomposition [14, 15], ionic liquid-assisted synthesis [16], hydrothermal method [4, 17, 18], co-precipitation method [19–21], and polyol [9, 10]. Recently, the use of metal–organic frameworks for the synthesis of metal oxides has gained attention as it helps to mitigate the problem of surface oxidation faced by various chemical methods [22]. Thermolysis/pyrolysis of MOFs provides a facile and scalable route to the synthesis of functional metal oxides with unique physicochemical and electronic properties [23–25]. Fe(MOF) derived α-Fe_2O_3 have been explored as functional materials in recent times in catalysis [26], adsorption [24], and gas sensing [25]. The use of MOFs as precursors for metal oxides leverages the unique structural and chemical properties of MOFs to generate materials with improved functionality and performance [22, 27–30]. Therefore, by leveraging the unique properties of Fe(MOF), α-Fe_2O_3 with tailored structure and different functional composition can be obtained, creating a facile route for obtaining materials with enhanced properties and suitability for various applications [26].

In nanocrystals, significant intrinsic strains are observed due to size confinement. The source of this lattice strain could be stacking faults, dislocation density, grain boundary junction, or point defect [31]. This intrinsic strain could be modulated through different synthesis factors such as annealing temperature, pH, and precursor type [32]. The XRD peak profile provides a significant route to evaluate the intrinsic strain in a crystal from the broadening of XRD peaks, which is a consequence of the finite size effect and the intrinsic strain resulting from size confinement [33]. Therefore, XRD peak profile analysis could offer an indirect route in estimating crystal properties such as size, intrinsic strain, and elastic properties such as energy density and stress. This can be achieved through several empirical analyses such as the Balza method, Williamson–Hall (W-H) analysis, and Warren-Averbach method. The W-H analysis is, however, very easy as it utilizes the full-width half-maximum (FWHM) of the XRD diffraction peaks.

Until now, limited attention has been paid to the influence of annealing temperature on the microstructural parameters and crystal defects of metal oxides obtained from the pyrolysis of MOFs. While most studies have paid attention only to the crystallite size, parameters such as lattice stress, crystal defects, and deformation energy density have not received much attention. Studying these parameters could, however, provide additional information on metal oxides as they greatly influence the physical properties of the material.

In this present study, the influence of annealing temperature on the microstructural properties of Fe_2O_3 obtained from the pyrolysis of Fe-MIM MOF is presented. Using XRD profile analysis methods such as modified Scherrer, W-H analysis, size strain plot, and Halder-Wagner methods (W-H), a comparative study of these materials is studied. Furthermore, morphological analysis was performed using transmission emission spectroscopy and electron dispersion spectroscopy of the obtained materials. The influence of the microstructural characteristics of the materials on the optical properties was further explored.

2. Methodology

The 2-methyl imidazole (MIM)(95%), iron nitrate pentahydrate (98%), and ethanol (99.9%) used in the synthesis of the materials were obtained from Sigma Aldrich, South Africa, and were used without further purification.

2.1. Synthesis of ZIF-8 like Fe-MIM MOF and Fe_2O_3 nanoparticles

For the synthesis of Fe-MIM, the method reported by Rahim, Yusuf (34) was employed with slight modification. In a typical synthesis, 1 mmole of iron nitrate pentahydrate and 8 mmole of 2-methylimidazole were dissolved in 15 mL of methanol. Under magnetic stirring, the 2-methylimidazole solution was added into the iron nitrate solution dropwisely, and the mixture was allowed to stir for 24 h. The obtained precipitate was washed and dried under a vacuum. For the synthesis of Fe_2O_3 nanoparticles, 100 mg of the MOF was measured into a ceramic crucible, after which it was transferred into a furnace, and heated at the desired temperature for 6 h. The samples heated at 800, 900, and 1000 °C are hereafter referred to as Fe_2O_3-800, Fe_2O_3-900, and Fe_2O_3-1000, respectively. After the heating, the samples were allowed to cool to room temperature and stored in a dry cool place.

2.2. Characterization of Fe-MIM and Fe_2O_3 nanoparticles

The x-ray crystallographic data were collected using a d8 Advanced XR diffractometer with Cu Kα radiation ($\lambda = 154.18$ pm). Morphological properties were examined using scanning electron microscopy (SEM) and transmission electron microscopy (TEM) on a TECNAI G2 (ACI) instrument (Hillsboro, OR, USA) with an accelerating voltage of 200 kV. The Fourier-transformed infrared (FTIR) spectra were recorded with a spectroquant® 300 spectrophotometer. UV–vis data were obtained using a Cary 60 UV–vis spectrometer (Agilent Technologies, Malaysia). For the SEM, TEM and UV–vis analyses ethanol was used as solvent.

3. Results and discussion

3.1. Structural analysis

Figure 1 shows the XRD and FTIR spectra of Fe-MIM obtained through a facile hydrothermal synthetic route. The Fe-MIM shows XRD pattern similar to that of ZIF-8 as reported by Jia, Cao (35) and Fe (II) analogue of ZIF-8 reported by Lopez-Cabrelles, Romero (36). The FTIR spectra (figure 1(b)) confirmed the formation of the Fe-MIM as an analogue of ZIF-8, with the C–H bond vibration observed at 2958 cm^{-1}. Furthermore, vibrational frequencies for C=N, C-N and Fe-N bonds were observed at 1617, 1365, and 600 cm^{-1}, respectively [34].

The XRD patterns of Fe_2O_3 obtained by the thermal decomposition of Fe-MIM at 800, 900, and 1000 °C are shown in figure 2. The XRD pattern gives information on the crystallinity and crystal system of the obtained Fe_2O_3. All the diffraction peaks could be indexed to the rhombohedral α-Fe_2O_3 phase [35]. The obtained Fe_2O_3 nanoparticles were pure and showed high crystallinity. The intensity of the main peak shows an apparent

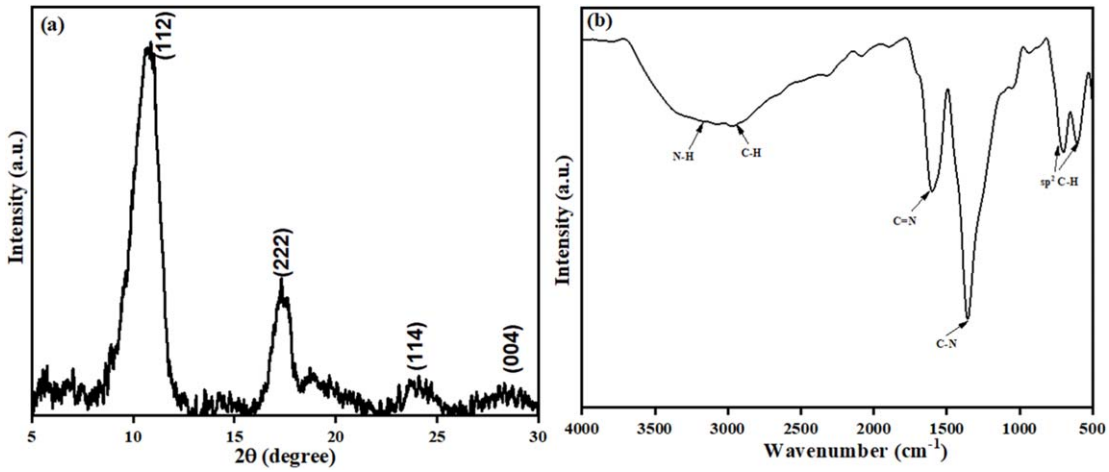

Figure 1. (a) XRD pattern and (b) FTIR spectra of ZIF-8 like Fe-MIM MOF.

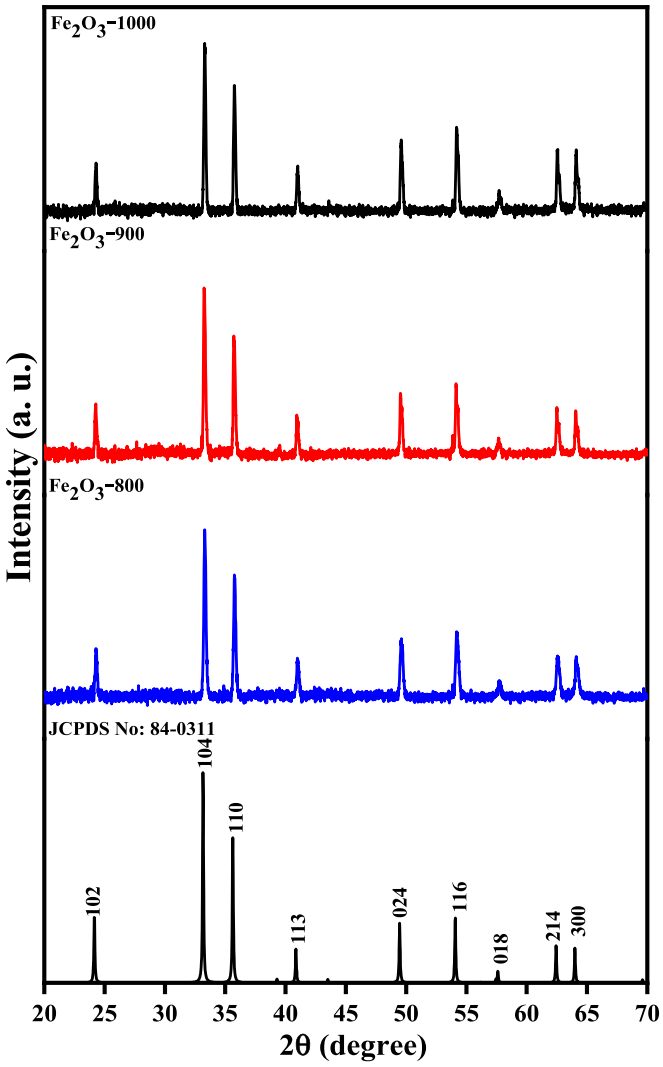

Figure 2. XRD pattern of Fe_2O_3-800, Fe_2O_3-900, and Fe_2O_3-1000.

increase with temperature, implying improved crystallinity at higher temperatures. The crystallinity followed the order Fe_2O_3-1000 > Fe_2O_3-900 > Fe_2O_3-800. High-temperature treatment has been observed to enhance crystallinity by improving atomic mobility and defect reduction [36]. A similar observation was reported for

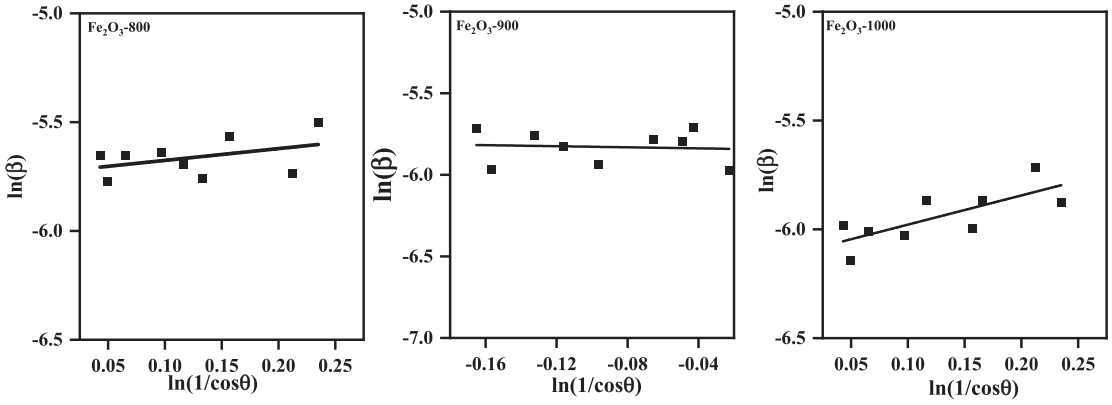

Figure 3. Linear plots of modified Scherrer equation for Fe_2O_3-800, Fe_2O_3-900, and Fe_2O_3-1000.

ZnO obtained through the sol–gel method and annealed at varying temperatures [37]. Furthermore, the full-width half-maximum (FWHM) of the main peak $2\theta = 33.5$ decreased as the annealing temperature increased. This further affirms the increase in crystallinity of the Fe_2O_3 nanoparticles and the presence of fewer defects in the crystal structure with an increase in annealing temperature. The diffraction data employed for calculating the crystallite size and intrinsic strain are discussed in the following sections.

3.1.1. The modified Scherrer method

Usually, the crystalline size of a material is determined using Scherrer's formula, which is based on diffraction peak broadening arising from the size and intrinsic strain effects. To account for physical and instrumental broadening, the diffraction peak broadening is corrected using the following equation [38, 39]:

$$\beta_d^2 = \beta_m^2 + \beta_i^2, \tag{1}$$

where β_d is the corrected broadening, β_m is the measured broadening and β_i is the instrumental broadening. The physical broadening of the samples and instrumental broadening obtained from the Al_2O_3 standard were measured through FWHM, and the corrected physical broadening was utilized in calculating the crystallite size using the Scherrer's equation [40, 41]:

$$D = \frac{K\lambda}{\beta_d}\frac{1}{\cos\theta}, \tag{2}$$

where D, K, λ, and θ represent the average crystallite size (nm), shape factor, wavelength of x-rays, and Bragg angle, respectively. Usually, the most intense peak is used in most studies to estimate the average crystalline size; however, to reduce the sum of absolute error, the modified Scherrer formula (equation (3)) was suggested by Monshi, Foroughi (45), which gives a more accurate estimate of the crystallite size from some or all of the diffraction peaks.

$$\ln\beta = \ln\left(\frac{K\lambda}{D}\right) + \ln\left(\frac{1}{\cos\theta}\right), \tag{3}$$

From equation (3), a plot of $\ln\beta$ against $\ln\left(\frac{1}{\cos\theta}\right)$ gives a straight line with an intercept $\ln\left(\frac{K\lambda}{D}\right)$. Figure 3 shows the graph of $\ln\beta$ versus $\ln\left(\frac{1}{\cos\theta}\right)$ for Fe_2O_3-800, Fe_2O_3-900, and Fe_2O_3-1000 obtained from all the experimental points from the XRD peaks of the samples. The average crystallite size estimated from the intercept was 44.5 nm, 50.0 nm, and 65.3 nm, respectively.

3.1.2. The Williamson–Hall analysis

The sole consideration of the influence of crystal size on XRD peaks broadening by the Scherrer method implies that it does not offer information on the internal lattice strain, which could arise from grain boundary, stacking faults, triple joints, or point defects in crystals [42, 43]. Therefore, methods such as Warren-Averbach and Williamson–Hall (W-H) analysis are used to estimate the contribution of intrinsic strain to XRD peaks broadening. The W-H analysis is the most explored among the methods because of its simplicity and usefulness in determining several crystal properties [44]. According to this model, the total peak broadening can be attributed to contributions from the size and microstrain of the crystal (equation (4)).

$$\beta_{total} = \beta_{size} + \beta_{strain} \tag{4}$$

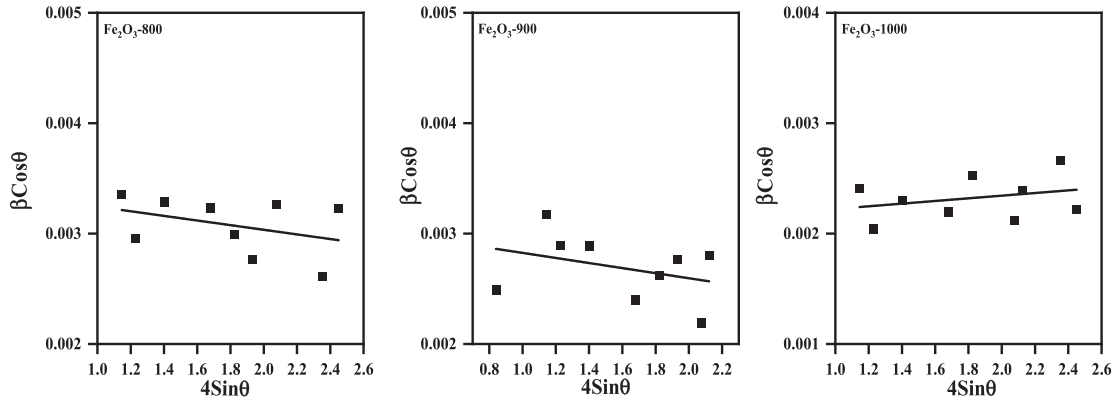

Figure 4. Linear plots of the UDM model for Fe_2O_3-800, Fe_2O_3-900, and Fe_2O_3-1000.

To estimate the crystallite size and microstrain in the Fe_2O_3 nanoparticles, three modified W-H equations–uniform deformation model (UDM), uniform stress deformation model (USDM), and uniform deformation energy density model (UDEDM)–were explored.

3.1.2.1. Uniform deformation model (UDM)

Despite the imperfection of nanocrystals, the UDM assumes the uniformity of strain in all crystallographic directions. Implying that the strain that influences XRD profile broadening is considered isotropic. The broadening induced by the strain (β_{strain}) can be expressed as follows:

$$\beta_{strain} = 4\epsilon \times \tan\theta \tag{5}$$

where ε is the microstrain. By combining β_{strain} (equation (5)) with β_{size} (equation (2)), the total broadening due to strain and size of any peak is:

$$\beta_{hkl} = \frac{K\lambda}{D\cos\theta} + 4\epsilon\tan\theta \tag{6}$$

By multiplying equation (6) with $\cos\theta$, the total broadening can be expressed as:

$$\beta_{hkl}\cos\theta = \frac{K\lambda}{D} + 4\epsilon\sin\theta_{hkl} \tag{7}$$

From equation (7), a plot of $\beta_{hkl}\cos\theta$ on the y-axis and $4\sin\theta_{hkl}$ on the x-axis gives a straight line with a slope equal to ϵ and the intercept on the y-axis is equal to $\frac{K\lambda}{D}$, from which D could be estimated. Figure 4 shows the UDM plots for the Fe_2O_3 samples, and the average crystal size was estimated to be 41.9, 47.4, and 72.0 nm for Fe_2O_3-800, Fe_2O_3-900, and Fe_2O_3-1000, respectively. The average intrinsic strain calculated from the intercept was -2.09×10^{-4}, -2.29×10^{-4}, and 1.20×10^{-4}, respectively. A positive strain is indicative of a tensile strain, while a negative strain signifies the presence of a compressive strain [42]. The reduction in the strain at higher annealing temperature shows a reduction in defect density, which is often correlated with a decrease in lattice strain.

3.1.2.2. Uniform stress deformation model (USDM)

If the strain in a crystal lattice is considered anisotropic, as observed in real crystals, the W-H equation must be modified to account for the anisotropic lattice deformation strain. The modified equation gives rise to the USDM model, which assumes a uniform deformation stress along all plane directions. According to Hooke's law, the linear relationship between stress and strain can be expressed by $\sigma = \varepsilon Y_{hkl}$, where σ, ε, and Y_{hkl} are the stress, anisotropic strain, and Young's modulus, respectively. Therefore, modifying equation (7) with Hooke's law expression yields the USDM equation as follows:

$$\beta_{hkl}\cos\theta_{hkl} = \frac{K\lambda}{D} + \frac{4\sigma\sin\theta_{hkl}}{Y_{hkl}} \tag{8}$$

For trigonal crystals, the Young's modulus is estimated by the expression:

$$\frac{1}{Y_{hkl}} = S_{11}l_1^4 + S_{22}l_2^4 + S_{33}l_3^4 + 2\left(S_{12} + \frac{S_{66}}{4}\right)l_1^2l_2^2 + 2\left(S_{13} + \frac{S_{44}}{2}\right)l_1^2l_3^2 + 2\left(S_{23} + \frac{S_{44}}{2}\right)l_2^2l_3^2$$

$$l_1 = \frac{h}{\sqrt{h^2 + k^2 + l^2}}, \quad l_2 = \frac{k}{\sqrt{h^2 + k^2 + l^2}}, \quad l_3 = \frac{l}{\sqrt{h^2 + k^2 + l^2}} \tag{9}$$

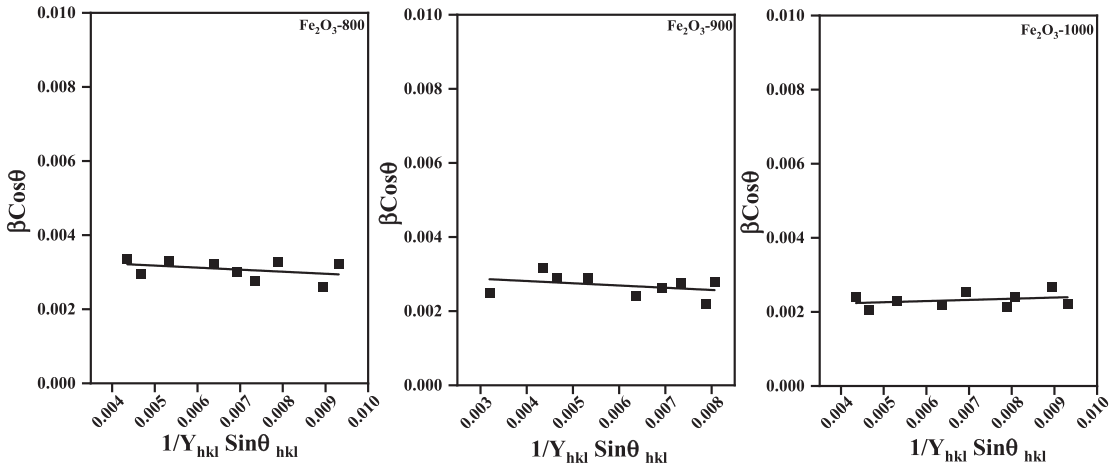

Figure 5. Linear plots of the USDM model for Fe_2O_3-800, Fe_2O_3-900, and Fe_2O_3-1000.

where h, k, and l are the Miller indices and the elastic compliances of trigonal Fe_2O_3. For Fe_2O_3, the elastic compliances S_{11}, S_{12}, S_{13}, S_{14}, S_{22}, S_{23}, S_{33}, S_{44} and S_{66}, are equal to 4.4×10^{-3}GPA^{-1}, -1.03×10^{-3} GPA^{-1}, -2.3×10^{-4} GPA^{-1}, -2.3×10^{-4} GPA^{-1}, 4.4×10^{-3} GPA^{-1}, -2.3×10^{-4} GPA^{-1}, 4.4×10^{-3} GPA^{-1}, 1.20×10^{-2} GPA^{-1}, and 2.7×10^{-3} GPA^{-1}, respectively [45, 46]. The average Y_{hkl} value for Fe_2O_3 estimated from the Miller indices using equation (9) was 263 GPa, which agrees with values reported in the literature [47, 48].

Figure 5 shows the plot of $\beta_{hkl} \cos\theta_{hkl}$ on the x-axis against $\frac{4 \sin\theta_{hkl}}{Y_{hkl}}$ on the y-axis for the Fe_2O_3 samples. The slope of the straight-line plot gives the value of σ, while the value of the crystal size can be estimated from the intercept, which is equal to $\frac{K\lambda}{D}$. The average crystal size for Fe_2O_3-800, Fe_2O_3-900, and Fe_2O_3-1000 were 41.9, 47.4, and 68.9 nm, respectively. Furthermore, the uniform stress (σ) obtained were 0.055, 0.060, and 0.032 GPa, respectively.

3.1.2.3. Uniform deformation energy density model (UDEDM)

Due to the imperfections in most crystals caused by dislocations, defects, and aggregation, the UDEDM model, which assumes the uniformity of deformation energy in all crystal directions, is often used as an alternative model to the UDM and USDM. For an elastic system, the relationship between energy density (u) and strain is defined by the Hooke's law: $u = \frac{\varepsilon^3 Y_{hkl}}{2}$. Consequently, equation (7) could be expressed as:

$$\beta_{hkl} \cos\theta_{hkl} = \frac{K\lambda}{D} + 4 \sin\theta_{hkl} \left(\frac{2u}{Y_{hkl}}\right)^{\frac{1}{2}} \tag{10}$$

To estimate the anisotropic energy density (u), a plot of $\beta_{hkl} \cos\theta_{hkl}$ on the x-axis against $4 \sin\theta_{hkl} \left(\frac{2}{Y_{hkl}}\right)^{\frac{1}{2}}$ gives a straight line with a slope equal to $u^{1/2}$, and the crystal size could be evaluated from the intercept which is equal to $\frac{K\lambda}{D}$ (figure 6). The value of u estimated from the slope of the plot was 5.52×10^{-6}, 0.051, and 0.036 GPa for Fe_2O_3-800, Fe_2O_3-900, and Fe_2O_3-1000, respectively. In addition, the crystal size estimated from the intercept was 41.9, 47.4 and 68.9 nm for Fe_2O_3-800, Fe_2O_3-900, and Fe_2O_3-1000, respectively.

3.1.3. Size-strain plot model

The size strain plot (SSP) analysis is a broadening analysis model that estimates the XRD peak profile as a blend of Gaussian and Lorentzian functions. A significant advantage of this model is that it eliminates the high peak overlap and low precision associated with higher-angle reflecting planes [49]. In this model, the crystallite size contribution to broadening is assigned a Lorentzian function, while the broadening due to strain is assigned the Gaussian function. The total peak broadening can then be expressed as the sum of broadening due to Gaussian (β_G) and Lorentzian (β_L) functions:

$$\beta_{total} = \beta_G + \beta_L \tag{11}$$

The SSP model is estimated according to the expression [50, 51]:

$$(d_{hkl} \beta_{hkl} \cos\theta)^2 = \frac{K\lambda}{D} (d_{hkl}^2 \beta_{hkl} \cos\theta) + \frac{\varepsilon^2}{4} \tag{12}$$

From equation (12), a plot of $(d_{hkl} \beta_{hkl} \cos\theta)^2$ on the y-axis against $d_{hkl}^2 \beta_{hkl} \cos\theta$ on the x-axis gives a straight line with a slope equal to $\frac{K\lambda}{D}$ and intercept equal to $\frac{\varepsilon^2}{4}$. Figure 7 shows the SSP plot for Fe_2O_3-800, Fe_2O_3-900, and Fe_2O_3-1000. The crystal size for Fe_2O_3-800, Fe_2O_3-900, and Fe_2O_3-1000 were estimated to be 43.2, 47.9, and

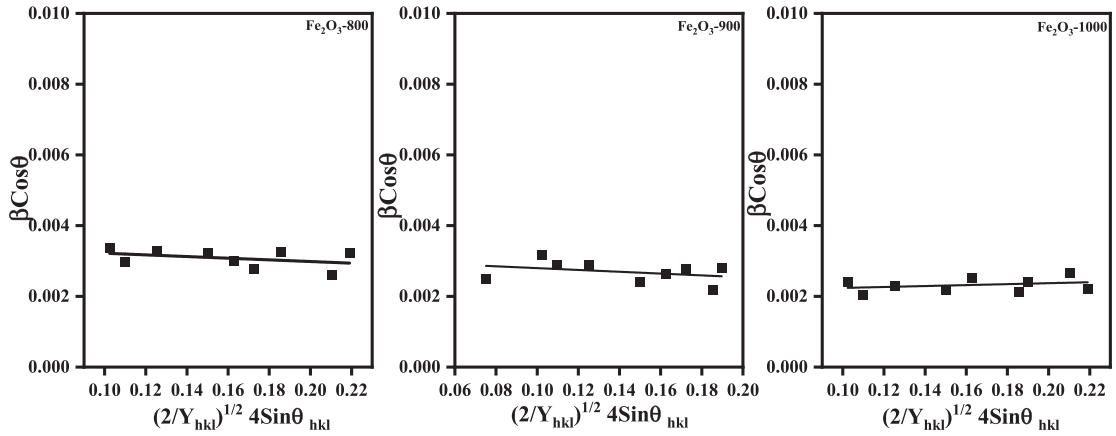

Figure 6. Linear plots of the UDEDM model for Fe_2O_3-800, Fe_2O_3-900, and Fe_2O_3-1000.

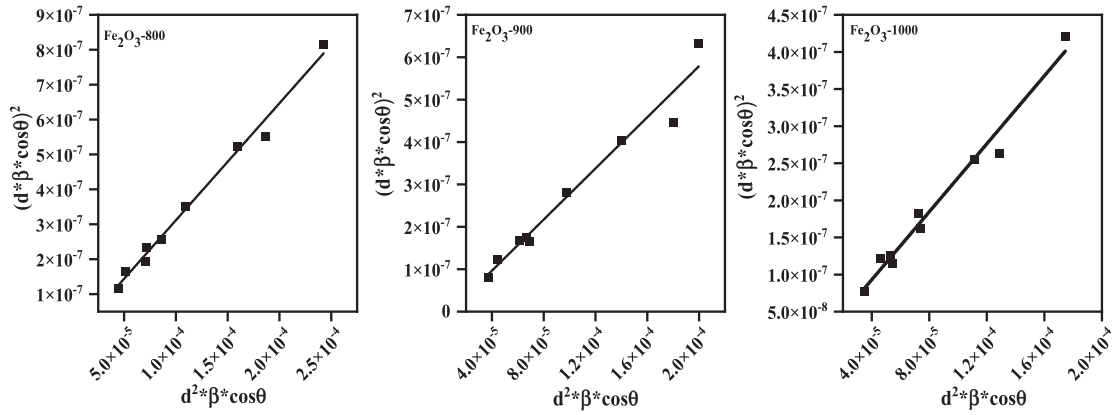

Figure 7. Linear plots of the SSP model for Fe_2O_3-800, Fe_2O_3-900, and Fe_2O_3-1000.

63.2 nm, respectively, while the strain (ε) was 3.03×10^{-4}, 3.1×10^{-4}, and 7.2×10^{-5}, for Fe_2O_3-800, Fe_2O_3-900, and Fe_2O_3-1000, respectively.

3.1.4. Halder-Wagner model

The H-W model is an alternative to the SSP model, as the XRD peaks broadening is assumed to be a Voigt symmetric function rather than the Gaussian and Lorentzian functions assumed by the SSP. The H-W model is desirable because the XRD peaks are neither Gaussian nor Lorentzian functions. Also, low and medium peaks receive more weight, while the overlap of diffraction peaks is minimized [50]. The H-W model is analyzed as a deconvolution of two Lorentzian and Gaussian functions. The FWHM of the physical profile could be expressed as:

$$\beta_{hkl}^2 = \beta_L \beta_{hkl} + \beta_G^2, \tag{13}$$

In the H-W model, the relationship between crystallite size and lattice strain is given by the expression:

$$\left(\frac{\beta^*}{d^*}\right)^2 = \frac{K}{D}\frac{\beta^*}{(d^*)^2} + (2\varepsilon)^2, \tag{14}$$

where $\beta^* = \beta_{hkl}\frac{\cos\theta}{\lambda}$ and $d^* = 2\frac{\cos\theta}{\lambda}$. To estimate the crystalline size and strain from equation (14), a linear equation is fitted to the plot of $\left(\frac{\beta^*}{d^*}\right)^2$ on the y-axis against $\frac{\beta^*}{(d^*)^2}$ on the x-axis. The obtained straight line as a slope and intercept equal to $\frac{K}{D}$ and $(2\varepsilon)^2$, respectively. Figure 8 shows the H-W plots for Fe_2O_3 samples. The estimated crystallite size was 43.1, 53.3, and 64.1 nm for Fe_2O_3-800, Fe_2O_3-900, and Fe_2O_3-1000, while the strain values were 4.97×10^{-4}, 2.16×10^{-4}, 1.19×10^{-4}.

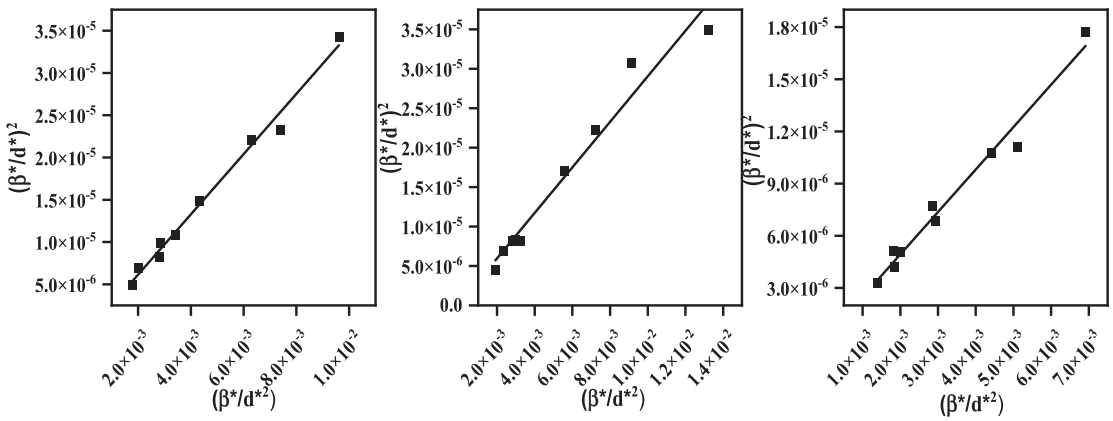

Figure 8. Linear plots of the H-W model for Fe_2O_3-800, Fe_2O_3-900, and Fe_2O_3-1000.

Table 1 gives the calculated average crystalline size and intrinsic strain of the Fe_2O_3 samples alongside other elastic parameters. The strain (ε) values calculated from the W-H analysis were similar for all three models; however, compared to the other models, the W-H analysis gave lower strain values, which can be attributed to the assumption of elastic constant anisotropy. Also, the average crystallite size calculated from all the models was similar. However, more disparity was observed in the values calculated for Fe_2O_3-1000, which could be attributed to the alteration in the strain in the sample. It is well established in the literature that values obtained from SSP and H-W models are more reliable because of the less significance given to high-angle refection and the close alignment of the data points with a linear fit [52].

3.2. Morphological study

TEM images were used to study the morphology of the Fe_2O_3 nanoparticles, while EDX was used to explore the elemental composition of the materials. The images of Fe_2O_3 samples are shown in figure 9. The TEM images show agglomerated round-shaped nanoparticles with a particle size that increased as the annealing temperature increased. High annealing temperature has been reported to promote grain size growth and aggregation in nanomaterials [53, 54]. This observed increase in particle size with annealing temperature is consistent with the results obtained from the structural analysis presented. The EDX images confirm the formation of pure Fe_2O_3 samples. Furthermore, an increase in the percentage composition of oxygen in the samples was observed to increase with annealing temperature, while the composition of iron decreased. This suggests the formation of Fe^{3+} vacancies and the formation of non-stoichiometric $Fe_2O_{3-}\alpha$ structures.

3.3. Optical properties

Figure 10 shows the UV–vis light absorption spectra and the Tauc plots for the Fe_2O_3 samples. Two transitions observed at 500–600 nm and 400–450 nm correspond to the indirect band edge and direct band edge, respectively [55]. The direct band edge corresponds to the transition from occupied O 2p to the empty Fe t_{2g}^* state, while the indirect band edge corresponds to the Fe $e_{.g.}$ state to the empty t_{2g}^* state transition. The absorption spectra of the three samples showed similar features. However, the intensity of light absorption decreased with an increase in annealing temperature, which can be ascribed to more defects in the samples obtained at lower temperatures. Also, the enhanced tailing of the samples prepared at 800 and 900 °C compared to the sample obtained at 1000 °C confirmed the presence of more defects in the samples obtained at lower temperatures. Transitions involving defects can result in absorption below the actual bandgap energy, resulting in tailing [56]. Furthermore, a blue shift in absorption edge to a higher wavelength was observed, suggesting an increase in band gap energy with an increase in annealing temperature due to increased crystallinity and reduced defects. This aligns with the observation from the XRD pattern of the samples, as an increase in the intensity of the XRD peaks was observed as the annealing temperature increased. Figure 10(b) shows the Tauc plot obtained from equation (15):

$$\alpha h\nu = A(h\nu - E_g)^n \tag{15}$$

The band gap energy was obtained from a plot of $(\alpha h\nu)^2$ against $h\nu$ by extrapolating the linear portion of the plot to $h\nu = 0$. The direct bandgap energy for Fe_2O_3-800, Fe_2O_3-900, and Fe_2O_3-1000 was evaluated as 1.75, 1.80, and 1.85 eV, respectively. The structural improvements—enhanced crystallinity, reduced defect density, and improved stoichiometry—serve as the foundation for the observed optical property changes. High annealing temperatures increase atomic mobility, enabling defect annealing and grain growth. The interplay between

Table 1. Estimated parameters for Fe_2O_3-800, Fe_2O_3-900, and Fe_2O_3-1000 nanoparticles.

	Modified scherrer method	Williamson–hall method									Size-strain plot		Halder-wagner method	
		UDM		USDM			UDEDM							
Sample	Size (nm)	Size (nm)	Strain (x 10^{-4})	Size (nm)	Strain ε (x 10^{-4})	Stress (GPA) (x 10^{-2})	Size (nm)	Strain ε (x 10^{-4})	Stress σ (GPA) (x 10^{-2})	Energy density u (GPA) (x 10^{-6})	Size (nm)	Strain ε (x 10^{-4})	Size (nm)	Strain ε (x 10^{-4})
Fe_2O_3-800	44.5	41.9	−2.90	41.9	2.13	5.5	41.9	2.05	5.4	5.52	43.2	3.03	43.1	4.97
Fe_2O_3-900	50.0	47.4	−2.29	47.4	2.28	6.0	47.4	2.24	5.8	6.6	47.9	3.10	53.3	2.16
Fe_2O_3-1000	65.3	72.0	1.20	68.9	1.22	3.2	68.9	1.14	3.0	1.7	63.2	0.7	64.1	1.19

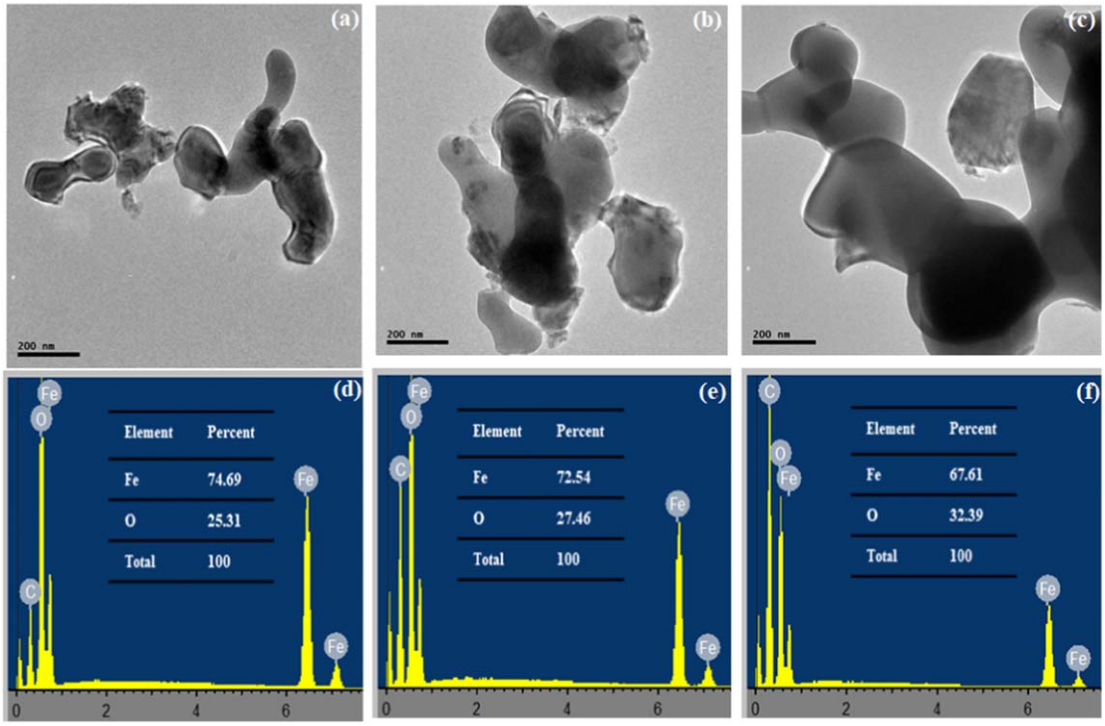

Figure 9. (a)–(c) TEM images and (d)–(e) EDX spectra of Fe_2O_3-800, Fe_2O_3-900, and Fe_2O_3-1000.

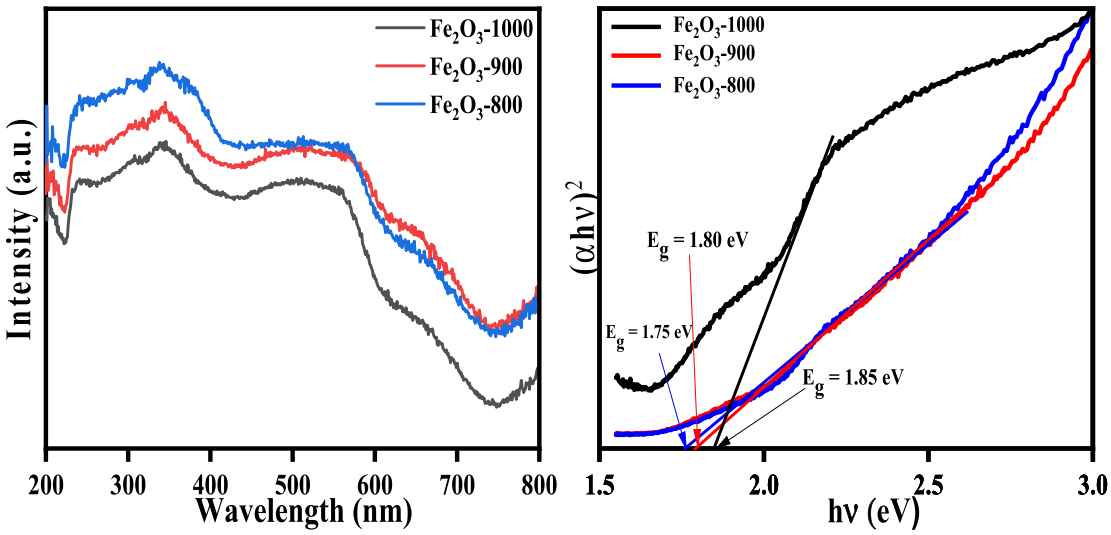

Figure 10. (a) UV-visible absorption spectra and (b) Tauc plots of Fe_2O_3-800, Fe_2O_3-900, and Fe_2O_3-1000.

reduced defects, enhanced crystallinity, and altered stoichiometry underlies the blue shift in the UV–vis absorption spectrum and the bandgap widening. These changes are consistent with structural improvements observed at higher annealing temperatures, showcasing how synthesis conditions can tailor the material properties for specific applications. This structural refinement reduces the density of mid-gap states and sharpens electronic transitions, as evidenced by the Tauc plot analysis showing increased bandgap values. This supports the earlier suggestion of band gap widening due to increased crystallinity and reduction in defects. High-temperature synthesis often influences defect density in nanomaterials [57].

To further confirm the level of defects in the obtained Fe_2O_3 samples, the Urbach energy (E_u) was calculated. The E_u indicates the overall disorder present in a crystal, and it shows the width of the traps in the crystal system [58]. These traps lead to the creation of localized states between the valence band and conduction bands. The E_u can be estimated using equation (16) [59]:

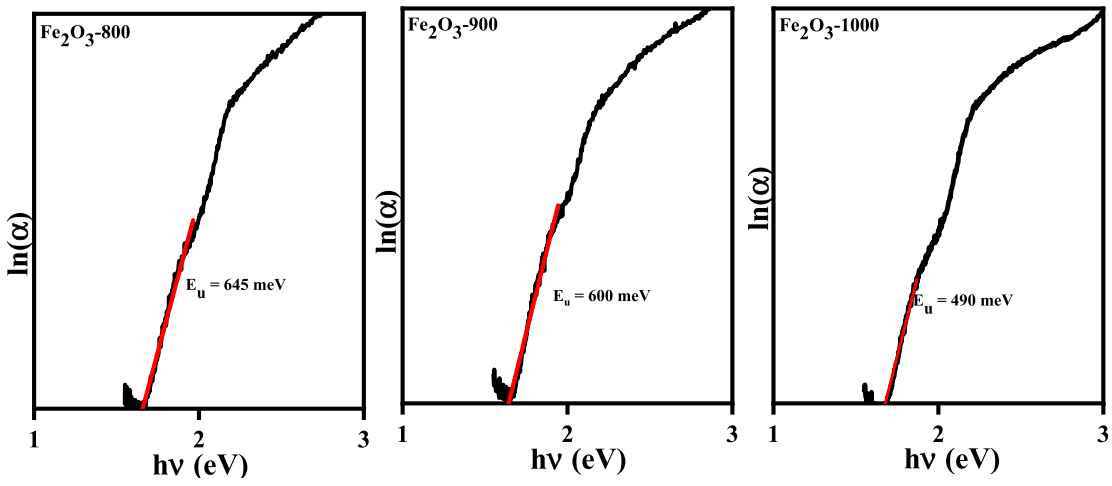

Figure 11. Urbach energy plot for Fe_2O_3-800, Fe_2O_3-900, and Fe_2O_3-1000.

$$\alpha = \alpha_o \exp\left(\frac{h\nu}{E_u}\right), \tag{16}$$

where, α is the absorption coefficient, $h\nu$ is the incident energy and α_o is a constant. The Eu is obtained by plotting ln (α) against $h\nu$ and fitting a linear equation on the linear portion of the curve, as shown in figure 11. The inverse of the slope of the linear fitting gives the value of Eu for the sample. The E_u for Fe_2O_3-800, Fe_2O_3-900, and Fe_2O_3-1000 was 645, 600, and 490 meV, respectively, which aligns with the inverse relationship between E_g and E_u and confirms the reduction in defects with higher annealing temperature [60]. Though the EDX analysis shows a higher amount of Fe vacancies in the samples as the annealing temperature increases, the E_u values show the presence of other defects, such as line defects at lower annealing temperatures. To affirm this, the dislocation density, a type of line defect for the samples, was estimated. The dislocation density is obtained from the expression in equation (17):

$$\rho_d = \frac{1}{D^2}, \tag{17}$$

where D is the crystallite size of the materials. The estimated dislocation density was 5.0×10^{-4}, 4.0×10^{-4}, and 2.3×10^{-4} line/nm^2 for Fe_2O_3-800, Fe_2O_3-900, and Fe_2O_3-1000, respectively. This confirms the presence of other defect types in the samples, which accounts for the higher overall defects in the samples obtained at lower temperatures.

4. Conclusion

In this study, we successfully synthesized α-Fe_2O_3 nanoparticles from the pyrolysis of ZIF-8 like Fe-MIM MOF and investigated the influence of annealing temperature on their microstructural, morphological, and optical properties. The XRD profile analysis using methods such as modified Scherrer, Williamson–Hall (W-H) size strain plot, and Halder-Wagner (H-W) revealed significant insights into the crystal structure, lattice strain, and crystallite size. Our results indicate that the crystallite size increases with annealing temperature while the intrinsic strain decreases. The TEM images demonstrated that the nanoparticles exhibited agglomerated round shapes, and the particle size increased with higher annealing temperatures, consistent with the XRD findings. The EDX analysis confirmed the purity of the Fe_2O_3 samples and suggested the formation of non-stoichiometric α-Fe_2O_3 structures with Fe^{3+} vacancies. Optical property analysis showed a blue shift in the absorption edge with increasing annealing temperature, indicating a widening band gap due to enhanced crystallinity and reduced defects. The direct bandgap energies for Fe_2O_3-800, Fe_2O_3-900, and Fe_2O_3-1000 were evaluated as 1.75, 1.80, and 1.85 eV, respectively.

These findings comprehensively explain how annealing temperature affects the structural and optical properties of α-Fe_2O_3 nanoparticles derived from MOFs. This study opens up potential avenues for optimizing the synthesis parameters to tailor the properties of α-Fe_2O_3 for specific applications in photocatalysis, gas sensors, lithium-ion batteries, and other fields.

Conflict of interest

Authors declare no conflict of interest.

Data availability statement

All data that support the findings of this study are included within the article (and any supplementary files).

ORCID iDs

Olalekan C Olatunde https://orcid.org/0000-0002-8245-0763
Tunde L Yusuf https://orcid.org/0000-0003-3419-9516
Damian C Onwudiwe https://orcid.org/0000-0002-2689-3981

References

[1] Mor G K, Prakasam H E, Varghese O K, Shankar K and Grimes C A 2007 *Nano Lett.* **7** 2356–64
[2] El-Sheikh S M, Harraz F A and Abdel-Halim K S 2009 *J. Alloys Compd.* **487** 716–23
[3] Mishra M and Chun D-M 2015 *Appl. Catal.*, A **498** 126–41
[4] Zheng X, Jiao Y, Chai F, Qu F, Umar A and Wu X 2015 *J. Colloid Interface Sci.* **457** 345–52
[5] Dong H, Zhang H, Xu Y and Zhao C 2015 *J. Power Sources* **300** 104–11
[6] Huang J, Yang M, Gu C, Zhai M, Sun Y and Liu J 2011 *Mater. Res. Bull.* **46** 1211–8
[7] Shahpari M, Behjat A, Khajaminian M and Torabi N 2015 *Sol. Energy* **119** 45–53
[8] Walter D 2006 *Thermochim. Acta* **445** 195–9
[9] Long N V, Yang Y, Thi C M, Hang B T, Cao Y and Nogami M 2015 *Colloid. Polym. Sci.* **293** 49–63
[10] Hang B T and Thang D H 2016 *J. Alloys Compd.* **655** 44–9
[11] Opuchovic O and Kareiva A 2015 *Ceram. Int.* **41** 4504–13
[12] Raja K, Jaculine M M, Jose M, Verma S, Prince A, Ilangovan K, Sethusankar K and Das S J 2015 *Superlattices Microstruct.* **86** 306–12
[13] Kayania Z, Afzala A, Butta M, Batoola I, Alia S and Riaz S *Mater. Today Proc.* **2** 5660–3
[14] Maji S K, Mukherjee N, Mondal A and Adhikary B 2012 *Polyhedron* **33** 145–9
[15] Al-Gaashani R, Radiman S, Tabet N and Daud A 2013 *J. Alloys Compd.* **550** 395–401
[16] Xu L, Xia J, Wang K, Wang L, Li H, Xu H, Huang L and He M 2013 *Dalton Trans.* **42** 6468–77
[17] Liu S, Sun Y-H, Dong P-P and Nan J-M 2015 *Materials Science and Engineering:* B **202** 15–24
[18] Khalil N, Wahsh M and Saad E E 2015 *J. Ind. Eng. Chem.* **21** 1214–8
[19] Sivakumar S, Anusuya D, Khatiwada C P, Sivasubramanian J, Venkatesan A and Soundhirarajan P 2014 *Spectrochim. Acta, Part* A **128** 69–75
[20] Farahmandjou M and Dastpak M 2018 *Physical Chemistry Research* **6** 713–20
[21] Ahmed S, Yoon W, Jo H, Irshad M, Khan M K and Kim J 2024 *Chem. Eng. J.* **499** 156104
[22] Das R, Pachfule P, Banerjee R and Poddar P 2012 *Nanoscale* **4** 591–9
[23] Sahoo S, Kumar R, Dhakal G and Shim J-J 2023 *Journal of Energy Storage* **74** 109427
[24] Gupta N K, Bae J and Kim K S 2021 *J. Environ. Chem. Eng.* **9** 106195
[25] Wei Q, Sun J, Song P, Yang Z and Wang Q 2020 *J. Alloys Compd.* **831** 154788
[26] Wu H, Lai L, Li Z, Hu J, Zhang L, Younas W and Liu Q 2023 *Catalysis Science & Technology* **13** 6635–9
[27] Wu H B, Wei S, Zhang L, Xu R, Hng H H and Lou X W 2013 *Chemistry* **19** 10804–8
[28] Yu C *et al* 2018 *J. Mater. Chem.* A **6** 8396–404
[29] Farisabadi A, Moradi M, Hajati S, Kiani M A and Espinos J P 2019 *Appl. Surf. Sci.* **469** 192–203
[30] Shen L, Liang R and Wu L 2015 *Chin. J. Catal.* **36** 2071–88
[31] Islam M A, Hossain A, Ahsan M Z, Bally M A A, Ullah M S, Hoque S M and Khan F A 2022 *RSC Adv.* **12** 8502–19
[32] Nath D, Singh F and Das R 2020 *Mater. Chem. Phys.* **239** 122021
[33] Manh D H, Ngoc Nha T T, Hong Phong L T, Nam P H, Thanh T D and Phong P T 2023 *RSC Adv.* **13** 25007–17
[34] Hao C, Zhou D, Xu J, Hong S, Wei W, Zhao T, Huang H and Fang W 2021 *J. Mater. Sci.* **56** 9434–44
[35] Li X, Wei W, Wang S, Kuai L and Geng B 2011 *Nanoscale* **3** 718–24
[36] Girard M, Combeaud C and Billon N 2021 *Polymer* **230** 124078
[37] Shivaraj B W, Murthy H N N, Krishna M and Satyanarayana B S 2015 *Procedia Materials Science* **10** 292–300
[38] Yogamalar R, Srinivasan R, Vinu A, Ariga K and Bose A C 2009 *Solid State Commun.* **149** 1919–23
[39] Delhez R, de Keijser T H and Mittemeijer E J 1982 *Fresenius' Zeitschrift für analytische Chemie* **312** 1–16
[40] Bindu P and Thomas S 2014 *Journal of Theoretical and Applied Physics* **8** 123–34
[41] Khorsand Zak A, Abd. Majid W H, Abrishami M E and Yousefi R 2011 *Solid State Sci.* **13** 251–6
[42] Rabiei M, Palevicius A, Monshi A, Nasiri S, Vilkauskas A and Janusas G 2020 Comparing methods for calculating nano crystal size of natural hydroxyapatite using x-ray diffraction *Nanomaterials [Internet]* **10**
[43] Balzar D and Ledbetter H 1993 *J. Appl. Crystallogr.* **26** 97–103
[44] Warren B E and Averbach B L 1952 *J. Appl. Phys.* **23** 1059
[45] Allen J 1973 *Phys. Rev.* B **8 7** 3224
[46] Haynes W M 2015 *CRC Handbook of Chemistry and Physics* 96th Edition (CRC Press)
[47] Chicot D, Mendoza J, Zaoui A, Louis G, Lepingle V, Roudet F and Lesage J 2011 *Mater. Chem. Phys.* **129** 862–70
[48] Ouglova A, Berthaud Y, François M and Foct F 2006 *Corros. Sci.* **48** 3988–4000
[49] Sundaram P S, Sangeetha T, Rajakarthihan S, Vijayalaksmi R, Elangovan A and Arivazhagan G 2020 *Physica* B **595** 412342
[50] Tatarchuk T, Bououdina M, Macyk W, Shyichuk O, Paliychuk N, Yaremiy I, Al-Najar B and Pacia M 2017 *Nanoscale Res. Lett.* **12** 141

[51] Mangavati S, Pal A, Rao A, Jiang Z-Z and Kuo Y-K 2022 *J. Phys. Chem. Solids* **160** 110301
[52] Motevalizadeh L, Heidary Z and Abrishami M E 2014 *Bull. Mater. Sci.* **37** 397–405
[53] Muthee D K and Dejene B F 2021 *Heliyon* **7** e07269
[54] Umar A, Kumar R, Kumar G, Algarni H and Kim S H 2015 *J. Alloys Compd.* **648** 46–52
[55] Qin Y X, Yang Z Z, Wang J J, Xie Z Y, Cui M Y, Tian C M, Du Y G and Zhang K H L 2019 *Appl. Surf. Sci.* **464** 488–93
[56] Choudhury B, Dey M and Choudhury A 2013 *International Nano Letters* **3** 25
[57] Fuhr A S, Sumpter B G and Ganesh P 2023 *Frontiers in Nanotechnology* **5** 1291338
[58] Rambadey O V, Kumar A, Sati A and Sagdeo P R 2021 *ACS Omega* **6** 32231–8
[59] Norouzzadeh P, Mabhouti K, Golzan M and Naderali R 2020 *Optik* **204** 164227
[60] Nazari N, Golzan M M and Mabhouti K 2024 *Sci. Rep.* **14** 6407